Monitoring Freeze-Thaw State by Means of GNSS Reflectometry: An Analysis of TechDemoSat-1 Data

Davide Comite, *Senior Member, IEEE*, Luca Cenci, Andreas Colliander, *Senior Member, IEEE*, and Nazzareno Pierdicca, *Senior Member, IEEE*

***Abstract*—The article of the freeze/thaw dynamic of high-latitude Earth surfaces is extremely important and informative for monitoring the carbon cycle, the climate change, and the security of infrastructures. Current methodologies mainly rely on the use of active and passive microwave sensors, while very few efforts have been devoted to the assessment of the potential of observations based on signals of opportunity. This article aims at assessing the performance of spaceborne Global Navigation Satellite System Reflectometry (GNSS-R) for high-spatial and high-temporal resolution monitoring of the Earth-surface freeze/thaw state. To this aim, reflectivity values derived from the TechDemoSat-1 (TDS-1) data have been collected and elaborated, and thus compared against the soil moisture active passive (SMAP) freeze/thaw information. Shallow subsurface soil temperature values recorded by a network of *in situ* stations have been considered as well. Even if an extensive and timeliness cross availability of both types of experimental data is limited by the spatial coverage and density of TDS-1 observations, the proposed analysis clearly indicates a significant seasonal cycle in the calibrated reflectivity. This opens new perspectives for the bistatic L-band high-resolution satellite monitoring of the freeze/thaw state, as well as to support the development of next-generation of GNSS-R satellite missions designed to provide enhanced performance and improved temporal and spatial coverage over high latitude areas.**

***Index Terms*—Bistatic radars, Freeze thaw (FT), global positioning system (GPS), GNSS reflectometry (GNSS-R), soil moisture active passive (SMAP), TechDemoSat-1 (TDS-1) mission.**

I. Introduction and Background

THE freeze/thaw (FT) state of the ground describes the seasonal landscape transition between predominantly frozen and thawed conditions [1]–[5]. It affects several environmental processes, occurring both at high elevations and at northern latitudes of the Earth surface [6]. The FT dynamic is considered an ecosystem variable important in many fields, such as hydrological, climatological, as well as for biogeochemical applications, and for infrastructure monitoring [6]–[8].

It is estimated that the world permafrost (defined as soil and rock that have been frozen for two years or more) holds almost double the amount of carbon than is currently in the atmosphere [9]–[11]. The global nitrous oxide budget is underestimated if FT induced emissions are not included in the calculation [12]. Since the FT state can be influenced by different factors (e.g., the land cover, soil moisture, and microclimate), it can be a highly heterogeneous process, both in time and in space.

Well-established and traditional methods to monitor the FT state over a certain region of interest (ROI) consist of *in situ* point-to-point measurements (see, e.g., [13]). They significantly limit the spatial coverage and the area that can effectively be studied at reduced costs and over continuous temporal intervals. The accuracy and large-scale monitoring of the FT state can be enhanced leveraging on spaceborne active and passive remote sensing techniques [3], [14]–[19]. However, current remote sensing methodologies still provide limited coverage and resolution performances, especially for applications requiring the study of regular short and mid-term variations of the FT dynamic.

Passive microwave radiometers are sensitive to FT changes, primarily because of soil permittivity variations, which can become significantly smaller in case of frozen soil. This causes an increase in the surface emissivity, which thus affects the brightness temperature measured at the receiving antenna. The latter is determined as the product of the surface emissivity and physical temperature, which can have contrasting effects [27], [28]. The most effective spectral region for microwave FT monitoring is the *L* band. It ensures, indeed, a good penetration and reduced influence of the vegetation, while keeping a reasonable spatial resolution (typically, about 30 km at nadir). Presently, FT fraction products based on the passive sensing are made available from soil moisture ocean salinity (SMOS), SAC/D Aquarius, and soil moisture active passive (SMAP) sensors with temporal resolution in the order of one to three days [15].

Scattered radar signals can also be very useful to monitor FT changes for the high spatial resolution, but also for the capability to measure permafrost deformation by interferometric techniques. In this case, the spatial coverage may be an issue [5], and wide swath modes have to be considered [21]. The SMAP

Manuscript received December 31, 2019; revised March 16, 2020; accepted April 3, 2020. Date of publication May 28, 2020; date of current version June 29, 2020. This work was supported by the ESA Contract 4000120299/17/NL/AF/hh "Potential of Spaceborne GNSS-R for Land Applications" Data of Chersky site were collected with funding from the US National Science Foundation under Grant PLR-1417745 and in part by the Jet Propulsion Laboratory, California Institute of Technology under a contract with the National Aeronautics and Space Administration. *(Corresponding author: Davide Comite.)*

Davide Comite and Nazzareno Pierdicca are with the Department of Information Engineering, Electronics and Telecommunications, "Sapienza" University, Rome 00184, Italy (e-mail: davide.comite@uniroma1.it; nazzareno.pierdicca@uniroma1.it).

Luca Cenci was with CIMA Research Foundation, 17100 Savona, Italy and with the Department of Information Engineering, Electronics and Telecommunications, Sapienza University, 00814 Rome, Italy. He is now with Serco Italia SpA, 00044 Frascati, Italy (e-mail: luca.cenci@serco.com).

Andreas Colliander Cenci is with the Jet Propulsion Laboratory, California Institute of Technology, Pasadena, CA 91109 USA (e-mail: andreas.colliander@jpl.nasa.gov).

Digital Object Identifier 10.1109/JSTARS.2020.2986859

radar was indeed conceived as a good compromise between the resolution and coverage [22], but unfortunately it stopped working few months after the satellite launch [5].

In principle, the reflection of signals of opportunity can also be profitably processed and analyzed to assess the sensitivity to the FT dynamic. The decrease of permittivity when the soil gets frozen, indeed, is expected to decrease the reflection around the specular direction, which represents the dominant contribution. Based on this simple mechanism, the reflection of the signal transmitted by Global Navigation Satellite Systems (GNSS) can be collected around the specular direction by an antenna looking downward [23]. The technique, known as GNSS Reflectometry (GNSS-R), has been recently tested from satellite platforms, such as the TechnDemoSat-1 (TDS-1) technological demonstrator mission and the Cyclone Global Navigation Satellite System (CyGNSS) NASA constellation made by eight satellites [24]–[26].

In case of GNSS-R acquisitions (and radar backscatter measurements), the signal is linked to permittivity changes, which are related to the temperature, soil constituents, and soil moisture. Snow cover effects should also be considered, although, as for dry snow conditions expected in winter, the snow is essentially transparent at *L* band.

As concerns the GNSS-R spatial resolution, signals over smooth land surfaces are generally assumed as mainly constituted by coherent reflections along the specular direction. At least for a flat profile, the signal mainly originates from the first Fresnel zone (FFZ) described by the transmitter–receiver configuration [23] (see also [29]–[31] for a discussion about these aspects). A contribution of the incoherent and diffuse scattering coming from the whole glistening zone does also exist [23], which is however less relevant for this investigation. In case of spaceborne receivers, which is the configuration considered in this article, the FFZ has a dimension of hundreds of meters and it is enlarged in the direction parallel to the orbit track according to the incoherent integration time [23], [29]. Conversely, the incoherent component discrimination in time and Doppler frequency determines a spatial resolution of about 25 km.

The GNSS-R temporal resolution, instead, depends on the characteristics of the mission. It can be significantly improved leveraging on GNSS constellations of transmitting satellites presently in place or in developing stage. On this basis, the GNSS-R technique enables the design of constellations of receiving-only systems, at reduced cost with respect to conventional space missions based on large platforms [25].

In the last few years, considerable research efforts have been done to model and understand the GNSS signals scattered over land [32]–[38].

The potential offered by the GNSS-R for spaceborne FT monitoring has been recently investigated in [28], where the authors carried out a theoretical and experimental analysis of data collected by the L-band receiver onboard the SMAP satellite, which was not originally designed for GNSS-R applications [15], [39], [40]. In [26] some SMAP observations over Arctic regions were also reported, although focusing the attention on melting effects and the spreading of waveforms due to subsurface scattering over Greenland continental ice sheets. The GNSS Transpolar Earth Reflectometry exploring System (G-TERN) mission, proposed as a candidate of the European Space Agency (ESA) Earth Explorer 9, includes FT state among its scientific objectives [41].

In this article, we empirically explore and describe the potential of a conventional GNSS-R system, i.e., TDS-1. We carry on an assessment of the impact of the FT dynamic on the TDS-1 signal, also including land-cover information of the ROI generating the GNSS reflections. In this respect, the proposed analysis should be considered complementary, but somehow more realistic with respect to the one proposed in [28], where the spatio-temporal sampling of SMAP observations is determined by the high-gain conically scanning antenna, in contrast with the low-gain nonscanning pattern of the TDS-1 GNSS-R mission [24].

The work is structured as follows: Section II describes the considered datasets, the postprocessing procedure, the selected ROI, and the general methodology. Section III presents the time-series analysis of SMAP data contrasted with the GNSS reflectivity over different bare and vegetated soils. Section IV outlines the comparison with near-surface *in situ* data. Conclusions and future developments are drawn in Section V.

II. Dataset and Methodology

GNSS-R data are collected by TDS-1 [24], which, among other sensors, carries on board the SGR-ReSI, (Space GNSS Receiver Remote Sensing Instrument), L-band receiver. The receiver is connected to two antennas, one looking downward for collecting the reflected signals and one upward collecting the L1A direct signals from the Global Positioning System (GPS) constellation. Both signals are processed by the correlator operating on board [24]. Assuming flat and/or smooth surfaces, which is the case for most of the areas under observation in this article, the reflected signal can be roughly assumed as generated by a region having dimensions of about 1 km $\times$ 7 km (i.e., the size of the FFZ enlarged along track according to the incoherent integration equal to 1 s) [24].

The temporal resolution depends on both the transmitting GPS satellite and the TDS-1 orbit, as well as the relevant acquisitions plan. This was not constant during the mission lifetime, and therefore the temporal resolution cannot be univocally defined. The GNSS-R CYGNSS constellation [25] have demonstrated the ability to operate with mean revisit time as short as 7 h operating a multireceiver constellation, whereas the TDS-1 single satellite exhibits appreciably longer temporal revisit. For this reason, the performance analysis proposed in this article has been constrained by the limited availability of experimental data.

During the first operational period, TDS-1 data have been acquired only few days every month. Only since the end of 2017, the mission started recording data continuously, even if some subsets have anyway undergone loss of data, mainly due to limited signal-to-noise ratio (SNR), quality flag constraints, and attitude issues. To overcome this limitation, the analysis is carried out here considering monthly average values, assuring each time an adequate coverage within the ROI (i.e., reflectivity samples of the order of 10–20 or more), averaging

latitude strips smaller than 3°. It should be mentioned that the TDS-1 collections considered in this article represent the longest GNSS-R dataset currently available, spanning over four years of operation.

To reduce calibration uncertainties and to achieve a higher SNR, reflections characterized by incidence angles greater than 30° or 45° have been removed from the dataset. The delay-Doppler Maps (DDMs) [23] have been used for computing the surface peak reflectivity and for estimating the noise level. Data marked by the quality flags *eclipse* or *direct signal in DDM* [42] have also been removed to deal with reliable data.

TDS-1 data were calibrated and preprocessed as described in [43], assuming the radar equation for a coherent signal, so that the received power P_r reflected by the surface along and around the specular direction is given by

$$P_{\mathrm{r}} = \frac{P_{\mathrm{t}} G_{\mathrm{t}}(\theta_{\mathrm{sp}}) G_{\mathrm{r}}(\theta_{\mathrm{sp}}) \lambda^2 \Gamma(\theta_{\mathrm{sp}})}{(4\pi)^2 (R_{\mathrm{t}} + R_{\mathrm{r}})^2} \tag{1}$$

where R_{r} is the distance from the receiver to the specular point (SP), R_{t} the one from the transmitter to the SP, λ is the wavelength, G_{t} and G_{r} are the gain of the transmitting and receiving (i.e., downlooking) antennas, and P_{t} the power transmitted by the GPS satellites. Γ is the surface (equivalent) reflectivity, which is a function of the incidence angle θ_{sp} at the SP. It should be mentioned that the incoherent scattering within the antenna footprint can also contribute to P_{r}. For this reason, the observable defined by (1) is referred to an *equivalent* reflectivity. The relative contribution from coherent and incoherent scattering depends on the receiver height, the topography, the surface roughness, and the vegetation cover. Over mainly flat areas, which have been selected in this work, the sensitivity to FT state should be mainly attributed to the specular reflection, which keeps a reasonable degree of coherence [44].

Most of the quantities required in (1) to retrieve $\Gamma(\theta)$ are available from the TDS-1 L1b products freely downloaded from the Merrbys web portal (http://merrbys.co.uk). To retrieve the power of the received signal, it is needed to remove the noise from the DDM peak, which was estimated from the first range lines of the DDM. The unknown quantity is the EIRP $= P_{\mathrm{t}} G_{\mathrm{t}}$ of the transmitter that was retrieved from the power of the direct signal available in the L1b product. The approach and its drawbacks are described in [43]. The reflectivity is finally retrieved from the peak power P_{r}^* of the DDM, the DDM noise N^*, the direct power P_{d}^*, and the related noise N_{d}^* through the following formula:

$$\Gamma\ (\theta) = \frac{(R_{\mathrm{r}} + R_{\mathrm{t}})^2}{R_{\mathrm{rt}}^2} \frac{(P_{\mathrm{r}}^* - N^*)}{(P_{\mathrm{d}}^* - N_{\mathrm{d}}^*)} \frac{G_{\mathrm{UP}}^{\mathrm{r}}}{G^{\mathrm{r}}}. \tag{2}$$

R_{rt}^2 is the distance from transmitter to receiver, the gain G^{r} toward the SP is extracted from the L1b product, whereas as for the upward antenna gain $G_{\mathrm{UP}}^{\mathrm{r}}$ we considered a constant nominal value of 4 dB, assuming a very wide pattern, according to the Merrbys documentation (http://merrbys.co.uk/). It is known that the calibration of GNSS-R data is an open issue, and this approach relies on some approximations as well, as discussed in [43] and [45].

The sensitivity of TDS-1 reflectivity to the FT dynamic is validated here by using additional independent datasets. The first is given by the FT fraction available in the SMAP L2 Radiometer Half-Orbit 36 km EASE-Grid Soil Moisture, version 5, downloaded from https://nsidc.org/data [46]. It provides a spatial resolution equal to 36 km and a temporal resolution of about 3 days. The FT fraction assumes variable ranges from 0 (thawed soil) to 1 (frozen soil) and it was initially retrieved from the SMAP radar data. Since the failure of the radar, it has been derived from external soil temperature ancillary data. It is a model-based quantity derived from the surface temperature using an average of two layers from the Global Modeling and Assimilation Office (GMAO) Goddard Earth Observing System Model, Version 5 (GEOS-5).

We have also considered the SMAP L3 Radiometer Global and Northern Hemisphere Daily 36 km EASE-Grid FT state, and specifically the Boolean value that indicates whether soil within a cell is frozen or thawed. This is a product derived from the brightness temperatures measured by the radiometer [5].

The SMAP FT fraction and FT state were organized to generate time series to be compared with the corresponding TDS-1 reflectivity considering the vegetation cover. More details about these aspects are given in Section III.

An independent validation is also provided through near-surface soil temperature data, sampled at 5 cm depth, and collected by three different networks of *in situ* stations located in Canada, Finland, Siberia, and Alaska [47], [48]. The ROIs for each area have been properly collected to grant a significant amount of TDS-1 data within the ROI, while, at the same time, providing proximity with *in situ* data and avoiding the presence of waterbodies. The latter are expected to generate a strong coherent reflection that can significantly affect the reflectivity level, leading to uncorrelated higher values both in the case of frozen bodies [34], [35] (low permittivity but essentially flat surfaces) and in case of thawed water bodies (higher permittivity).

III. Comparison With SMAP Data

The capability of GNSS data to monitor the FT dynamic is investigated here by comparing time series of monthly average reflectivity against monthly average of the SMAP FT fraction and FT state over the north region of the hemisphere (see Fig. 2). We have considered areas whose FT annual cycle was expected to be fairly homogeneous. To this aim, we have relied on the International Geosphere–Biosphere Programme (IGBP) land-cover classification derived from MODIS acquisitions (spatial resolution of 1 km) [49]. We have considered a few land cover classes, which have been reclassified in macro classes according to the rules reported in Table I (see [49] for the class definitions). The class of water in [49] has also been used to mask reflections that could have been contaminated by lakes or rivers. Therefore, the entire region under study has been partitioned in ROIs characterized by homogeneous land covers, according to the map. They are selected to be in similar ranges of latitude. The ROIs considered in this analysis are depicted in Fig. 1 using different colors.

The monthly average of the TDS-1 reflectivity values and of the SMAP FT fractions has been computed for each ROI (after

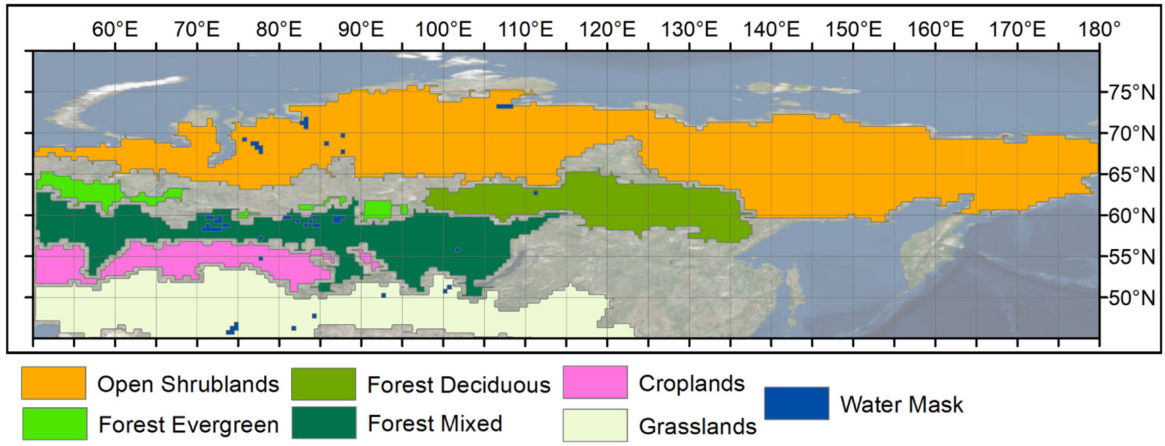

Fig. 1. Reclassified macro-land cover classes for continental Siberia considered for the time-series analysis of the SMAP FT product and the TDS-1 calibrated reflectivity.

TABLE I
LOOK-UP TABLE SHOWING THE RECLASSIFICATION OF THE ORIGINAL MODIS [49] LAND COVER CLASSES FOR THE CONTINENTAL SIBERIA INTO MACRO-CLASSES

Original land cover classes (MODIS database)	Reclassified macro land cover
Evergreen needleleaf forest	Forest evergreen
Deciduous needleleaf forest	Forest deciduous
Deciduous broadleaf forest	Forest deciduous
Mixed forest	Forest mixed
Open shrublands	Open shrublands
grasslands	Grasslands
croplands	Croplands

data averaging, reflectivity values were converted to decibel units). The considered time interval spans from the beginning of 2015 up to December 2018, when the TDS-1 mission completed its lifecycle. A percentage of the frozen pixels within each ROI, for the years 2017 and 2018, has been also computed from the FT state L3 SMAP product [51].

Fig. 2 reports the results of the time-series analysis assuming the land cover classification as in Table I (right column). The title of each subfigure, from (a) to (f), indicates the relevant class of vegetation. Some data points are missing because of the poor TDS-1 sampling during some months. A fairly good agreement between the oscillations of the TDS-1 reflectivity (green left axes) and the SMAP FT fraction (red right axes) has been achieved for some of the considered ROIs.

Fig. 2(a)–(c) and (e) (i.e., shrublands, forest deciduous, croplands, and forest mixed) shows a reflectivity dynamic range up to 8−10 dB; however, the average, maximum, and minimum values change according to the ROIs, which are characterized by different land cover and latitudes. As expected, lower reflectivity values associated with lower permittivity have been generally obtained in winter months, when the SMAP products indicate a higher fraction of frozen pixels, approaching in most cases 100% of frozen pixels in January. Higher reflectivity values, instead, have been mainly obtained in correspondence of a higher fraction of thawed pixels (higher permittivity). Two exceptions showing noisy temporal trends of Γ can be observed for the evergreen forest and the grassland. The former corresponds to the smaller ROI (see Fig. 1), so that the reflectivity profiles are noisier. Moreover, this is the class where a larger effect of the attenuation by vegetation and volume scattering is expected. The concurrence of these two factors may have led to the noisy profile, even if in the last year, when the TDS-1 acquisitions were almost systematic, a clearer signal is observed. As for the grassland, this is the most southernmost ROI, where the FT conditions are likely not homogeneously distributed in time and space. The spatial and temporal averaging over the entire grassland area has likely led to a poor seasonal signal for the mean monthly profile. A more accurate analysis would require a better spatial-temporal sampling, not available from TDS-1. It should be also mentioned that the GNSS-R reflections may exhibit fluctuations due to loss of coherence of the specular signal likely associated with calibration issues and/or topography.

IV. COMPARISON WITH *IN SITU* DATA

To enhance the understanding of the performance provided by the GNSS-R technique, we propose here a comparison with *in situ* networks of pointwise groundtruth data. A study is thus described to evaluate the correlation between near-surface (5 cm) temperature data and reflectivity values. Four different station networks located in the northern region of the Asian and American continents have been considered:

1) Finland, Sodankyla; lat: 67.37°, lon: 26.67°.
2) Canada, Kenaston; lat: 51.40°, lon: −106.45°.
3) Eastern Siberia, Chersky; lat: 68.75°, 161.48°.
4) Alaska, Bonanza Creek; lat: 64.69°, −148.32°.

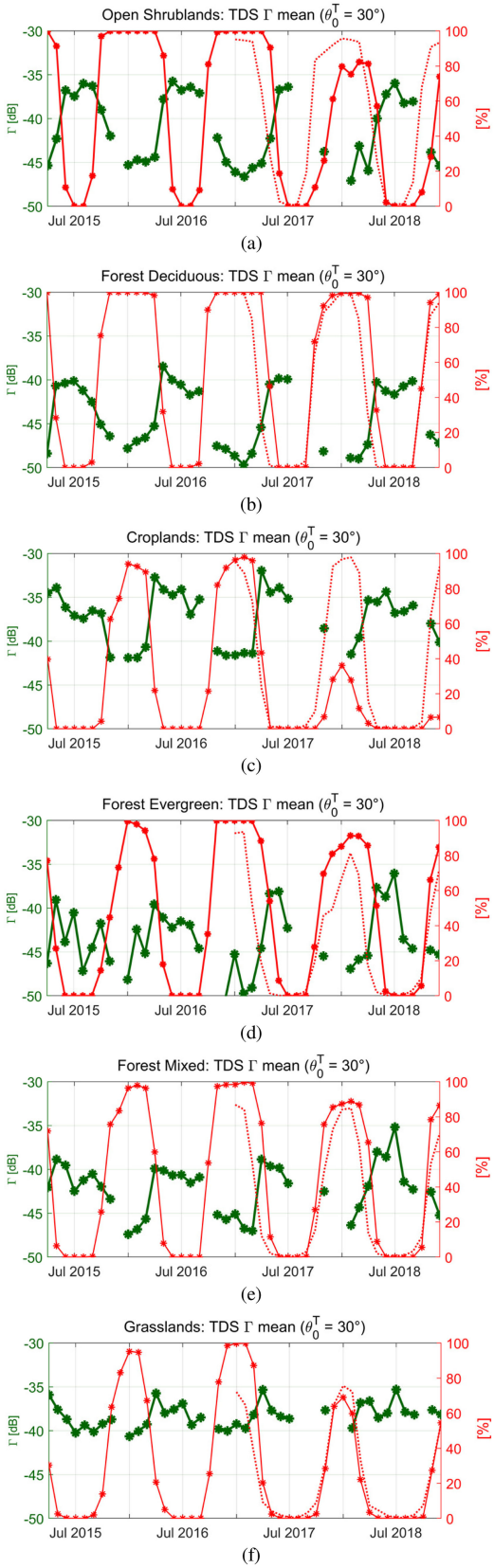

Fig. 2. Time-series analysis of the SMAP FT fraction (solid red curve, right axis) and percentage of frozen pixels (dotted red curve, right axis) versus the TDS-1 calibrated reflectivity (left axis). The relevant macro-area land-cover classes are reported in the subfigure title. θ_0^T indicates the upper bound of the considered incidence angles.

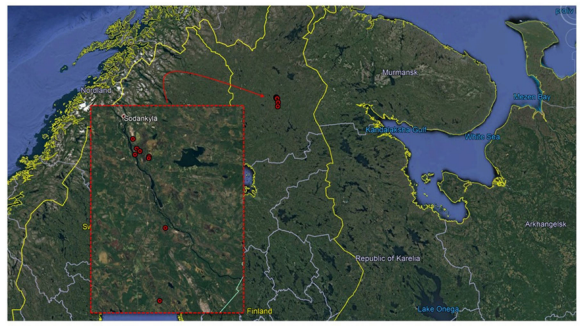

Fig. 3. Network of *in situ* stations located in Finland. A zoom-in view is shown by the red-dashed inset.

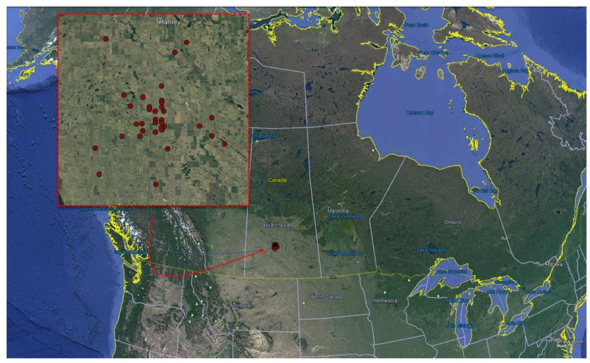

Fig. 4. As in Fig. 3 for Canada.

Fig. 5. As in Fig. 3 for Siberia.

The location of the considered macro regions is presented in Figs. 3–6. Four sets of ROIs (approximately rectangular) have been manually selected to provide a significant coverage of TDS-1 data, ensuring to include the locations of the ground stations. As mentioned, to deal with the limited availability of TDS-1 data within the ROIs during the entire lifetime of the mission, the reflectivity values have been averaged over time (within each month) and space (within the ROI). To perform a coherent comparison, the same averaging scheme has been applied to the local temperature data.

The ROIs have been postprocessed to assure the absence of water bodies within the polygons. To this aim, the water body masks provided in [52] have been dilated and resampled at the SP

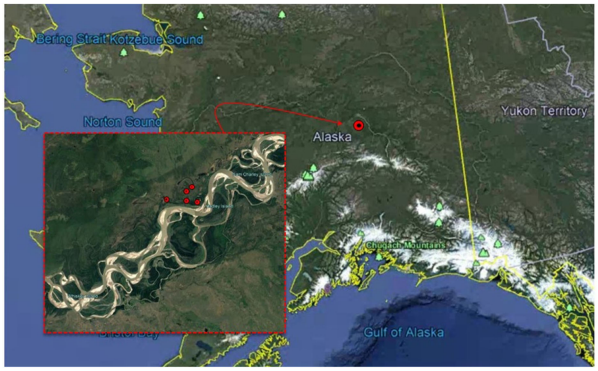

Fig. 6. As in Fig. 3 for Alaska.

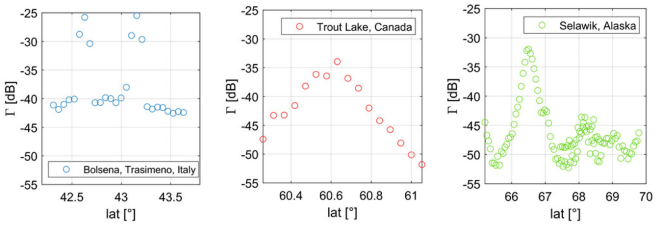

Fig. 7. TDS-1 reflectivity (in dB) of an orbit crossing three lakes at three different latitudes. (Note that two different Italian lakes are crossed by the SP in case (a), which correspond to the two peaks).

locations and used to remove possibly contaminated reflections. A rectangular buffer oriented along the track of the satellite, having dimension equal to 1 by 7 km, has been applied around the original water body to dilate it. The masking operation is particularly important for Finland, which presents a complex pattern of rivers and connected canals that can significantly affect the order of magnitude of the measured reflectivity. This is evident in case of liquid water (very high reflectivity), but also in frozen conditions, when the water bodies are expected to be much smoother than the soil. Assuming a relative permittivity equal to 3, variations of the order of 6–10 dB between the square module of the Fresnel reflection coefficient of mainly frozen flat surfaces can be straightforwardly calculated with respect to the one reduced by the surface roughness, as dictated by the geometric optics approach (see, e.g., [31]). In other words, despite the similarity of permittivity of frozen water and soil, the low roughness of frozen lake can produce reflectivity of 6–10 dB higher. This has been verified by analyzing the TDS-1 reflectivity [evaluated as given by (2)] achieved in February when crossing three different lakes at three different latitudes. They have been reported in Fig. 7 (see figure caption for all the relevant details). It is observed that when crossing the Italian lakes (the lowest latitude), the reflectivity presents two clear and strong peaks (determined by a flat surface with high dielectric constant). When crossing the frozen lakes in central Canada and Alaska, the reflectivity peak is still visible but reaches smaller values. This can be related to the flat iced surface with a smaller dielectric constant.

To provide an intuitive comparison with the local surface temperature given by the *in situ* probes, a reflectivity anomaly

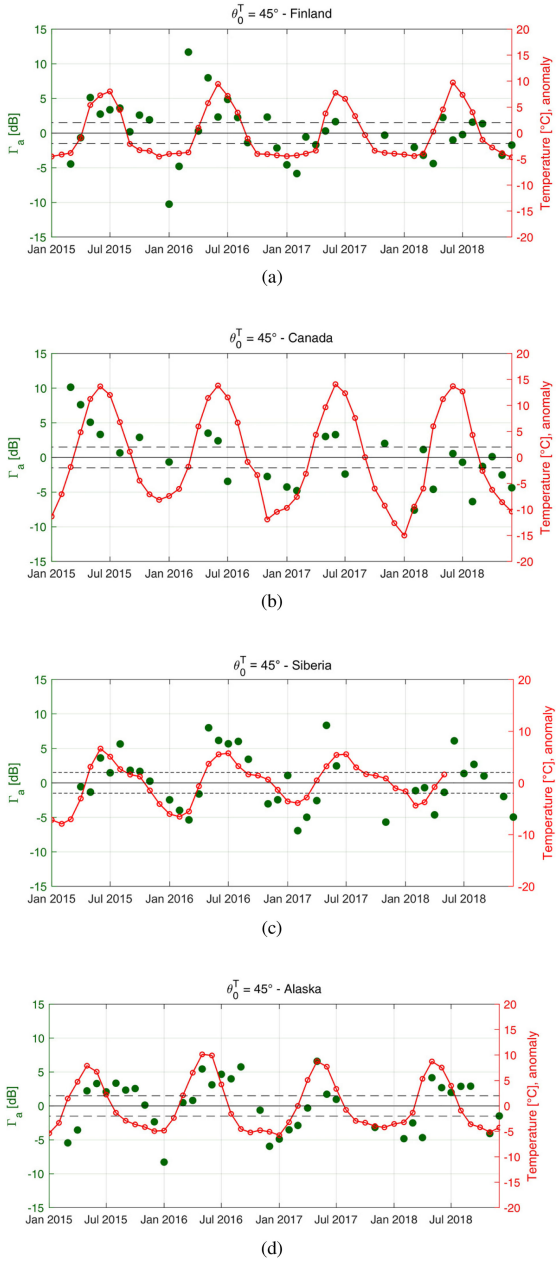

Fig. 8. Comparison with *in situ* near surface temperature data: time series of reflectivity anomalies and temperature. The title of each subfigure reports the ROI and the range of considered incidence angles. θ_0^T indicates the upper bound of the considered incidence angles. Reflectivity mean values: (a) −37 dB; (b) −39.8 dB, (c) −41 dB, (d) −40 dB. Temperature mean values: (a) 4 °C; (b) 5.6 °C, (c) −1.2 °C, (d) 3 °C.

is defined as follows for each ROI under consideration:

$$\Gamma_{a_{\mathrm{dB}}} = \Gamma_{m_{\mathrm{dB}}} - \langle \Gamma_{\mathrm{dB}} \rangle \tag{3}$$

where $\Gamma_{m_{\mathrm{dB}}}$ is the monthly averaged reflectivity within each ROI, evaluated through (2), and Γ_{dB} the corresponding global average of all values along the considered time frame. The same definition is applied for the temperature anomaly. The absolute value of the mean reflectivity over the time series (see Fig. 10 below) shows, in general, a significant dynamic range, with most of the data spanning values within about −45 and −35 dB.

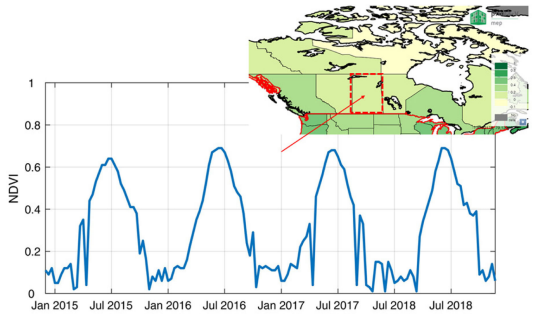

Fig. 9. Analysis of PROBA-V NDVI time series in the study area corresponding to the Canadian *in situ* network of stations used in the analyses presented in Fig. 8(b).

It is noted here that the reflectivity values within a ROI exhibit quite a large variability. This can be associated with intrinsic fluctuations of the signals discussed at the end of Section III [44] (sort of speckle noise), to calibration issues, as well as to the presence of surface inhomogeneities. Moreover, the reflections collected from different orbits do not regularly occur at the same point of the Earth surface. Then different SPs concur to successive monthly means, which is an additional cause of fluctuation in the data. These sources of variability are poorly mitigated by the incoherent averaging when the number of reflections within a ROI is not adequate and can significantly change from one month to another, as in the case of TDS-1 with limited duty cycle. This is certainly a weakness of spaceborne GNSS-R relying on a single platform.

The relevant time series patterns are reported in Fig. 8(a)–(d). The results generally show that negative anomalies are associated with frozen soil conditions (i.e., lowest temperature), whereas positive anomalies with thawed soil conditions (i.e., highest temperature). Transitional seasons, in which the temperature anomaly ranges between -2 and 2 °C, can produce results with a certain degree of uncertainty (e.g., a lower correlation between reflectivity anomalies and temperature). This may be due, besides the strong fluctuations discussed above, to the poor correspondence in space between reflections and ground probes.

By comparing the temperature dynamic range among the three different regions, it can be seen that, as expected, the ROI in Siberia shows the smaller temperature excursions, which is associated with a very good similarity with the measured reflectivity temporal profile. Peak of the anomaly can be observed in June and July, whereas clear minima are observed in January/February. The correlation among variations of the permittivity and FT state is apparent. Each point in the plot derives from averaging about ten reflections in most cases, with some exceptions, mainly in 2018. A similar behavior can be observed in Finland where, however, the variation of the reflectivity is narrower but also noisier, despite the larger number of averaged samples (around two hundred in this case). A point-by-point analyses have revealed that the scattering mechanism in that region can be significantly influenced by the dense network of water bodies, rivers, and streams, which are present in that region. We have verified that some small water bodies not connected to rivers have been missed by the water mask provided in [52].

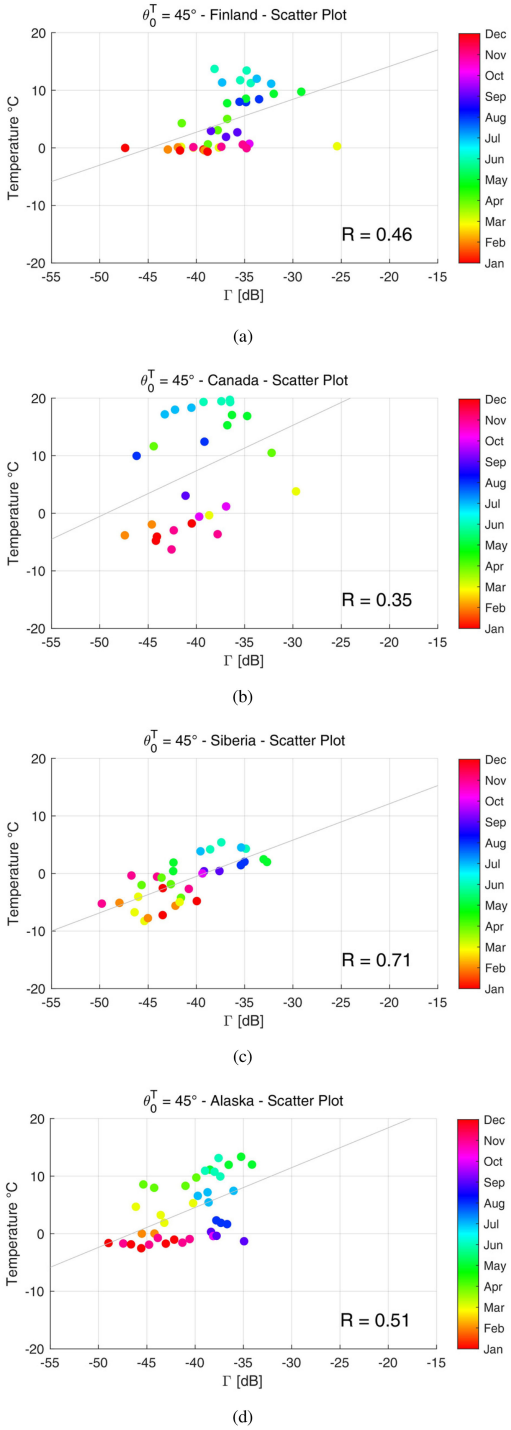

Fig. 10. Scatter plot for the data (absolute values, not anomalies) as in Fig. 8 with colors representing the relevant months. A least square line is also represented. θ_0^T indicates the upper bound of the considered incidence angles.

As concerns the ROI designed within the macro-area of Canada [see Fig. 8(b)], the temperature variation is stronger, followed by important variations of the anomaly. The number of averaged reflectivity values is around ten before 2018. Some transitions from warm to cold months can be observed in the reflectivity temporal profile (see for instance from January to July 2017), but the general trend is less distinct. Months

characterized by negative anomalies during the summer season were found [e.g., June/July in Canada, Fig. 8(b)]. Note that this is mainly an agricultural area, where significant changes of crop growing stage and soil moisture may undergo during the warm season. The comparison with the NDVI time series produced by using PROBA-V data [53] (see Fig. 9) proved that this behavior can be linked to high-normalized differential vegetation index (NDVI) values, that in turn can indicate the growth of the vegetation/crops and its attenuation of the reflected signal. The drying of soil toward mid-summer may be also another factor.

The pattern of the reflectivity anomaly over Alaska in Fig. 8(d) confirms a fair sensitivity to the temperature variation.

Fig. 10(a)–(d) present the same data in Fig. 8, but as scatter plots among the calibrated TDS-1 reflectivity and the temperature (absolute values in this case) over the ROI's described in Figs. 3–6. The colormap and the relevant labels identify the considered months. A least square fitting line and the corresponding correlation coefficients R are also reported. As is visible, a fair correlation can be observed between the two observables in Siberia and Alaska. In Canada, and partially in Finland, two correlated groups of points can be identified related to warm months (bluish points) and cold months (reddish points), respectively. This could be associated with the additional factors affecting the reflectivity already discussed, such as crop growing and soil moisture, and it deserves more investigations in the future.

V. Conclusion

The potential of spaceborne GNSS-R for the soil freeze/thaw monitoring at high latitudes was investigated in this article. Reflectivity values derived from TDS-1 acquisitions, collected within the period April 2015–December 2018, were calibrated and analyzed.

TDS-1 data were compared against the SMAP L2 freeze/thaw fraction and the SMAP L3 freeze/thaw state in Siberia, within homogeneous land cover classes. *In situ* data of the subsurface soil temperature, sampled at a depth of 5 cm, collected by three networks of *in situ* stations, located in Finland (Sodankyla), Eastern Siberia (Chersky), northeast of Canada (Kenaston), and Alaska (Bonanza Creek), were also compared with the anomaly of the reflectivity temporal patterns. Particular attention was devoted to the characterization of the land cover influence on the reflection of the GNSS-R signal and in particular to the influence of water bodies, either melt or iced.

The investigation demonstrates in many cases the similarity of the reflectivity monthly temporal profiles with those of the reference quantities considered in this article. The decrease of reflectivity of frozen soils and its increase in case of thawed soils is generally confirmed with a dynamic range up to 10 dB in the most favorable conditions. This demonstrates the potential of spaceborne GNSS-R to monitoring the FT soil state at high spatial resolution (of the order of few kilometers in case of scattering predominantly coherent).

Cases with poorer matching were also observed in some of the considered areas under test. It should be stressed that the proposed analysis was carried out using the TDS-1 data characterized by a discontinuous and nonuniform acquisition plan. This may have weakened the capability of spatio-temporal means to smooth fluctuations. Indeed, fluctuations are inherent to the GNSS-R technique, to the nonsystematic sampling of the surface, to the high sensitivity to some targets (e.g., water bodies), as well as to calibration issues. The vegetation cover affects the absolute value of the signal as well. Especially in agricultural areas, anomalous low reflectivity values in summer months were likely due to vegetation attenuation or dry soil conditions. Anomalous high reflectivity values in winter months are likely due to water bodies or small lakes not properly filtered out.

Taking in due consideration the intrinsic limits of the explored dataset, the article indicates that a GNSS-R mission based on a constellation of receiving-only small satellites, with a proper inclination of the orbital plane, can provide the needed coverage of the northern Earth hemisphere to fully exploit the potential of the technique and to improve the temporal resolution with respect to more conventional methods.

The article highlights the need of developing a proper absolute calibration approach, as well as models to predict the scattering generated at the receiver as a function of the permittivity variations, land cover, and topography. This is required to design a robust technique for the discrimination of the freeze-thaw state exploiting ancillary data or change detection methods. Future efforts to advance this method should also be focused on a more accurate characterization of the spatial resolution of the GNSS-R technique.

Acknowledgment

The authors would like to thank K. Rautiainen, Finnish Meteoregical Institute; A. Berg, University of Guelph; M. Loranty, Colgate University, and E. Euskirchen, Alaska Climate Adaptation Science Center, for providing *in situ* data. TechDemoSat-1 data were collected through the Merrbys portal at http://www.merrbys.org/. SMAP products were downloaded from https://nsidc.org/data.

References

[1] K. C. McDonald and J. S. Kimball, "Hydrological application of remote sensing: Freeze-thaw states using both active and passive microwave sensors," in *Encyclopedia of Hydrological Sciences. Part Five: Remote Sensing*. Hoboken, NJ, USA: Wiley, 2005.

[2] E. Podest, "Monitoring boreal landscape freeze/thaw transitions with spaceborne microwave remote sensing," Ph.D. dissertation, Univ. Dundee, Dundee, U.K., 2005.

[3] E. Rignot and J. B. Way., "Monitoring freeze–thaw cycles along North—South Alaskan transects using ERS-1 SAR," *Remote Sens. Environ.* vol. 49, no. 2, pp. 131–137, Aug. 1994.

[4] S. Kim, J. van Zyl, K. McDonald, and E. Njoku, "Monitoring surface soil moisture and freeze-thaw state with the high-resolution radar of the soil moisture active/passive (SMAP) mission," in *Proc. IEEE Radar Conf.*, May 2010, pp. 735–739.

[5] C. Derksen *et al.*,"Retrieving landscape freeze/thaw state from Soil Moisture Active Passive (SMAP) radar and radiometer measurements," *Remote Sens. Environ.*, vol. 194, pp. 48–62, Jun. 2017.

[6] Permafrost CCI Project, E. S. Agency, [Online]. Available: http://cci.esa.int/Permafrost, Accessed: Oct. 2019.

[7] H. Bergstedt and A. Bartsch, "Surface state across scales: Temporal and spatial patterns in land surface freeze/thaw dynamics," *Geoscience*, vol. 7, no. 3, 2017, Art. no. 65.

[8] J. Qi, P. A. Vermeer, and G. Cheng, "A review of the influence of freeze-thaw cycles on soil geotechnical properties," *Permafrost Periglacial Processes*, vol. 17, no. 3, pp. 245–252, Jul. 2006.

[9] K. Schaefer, T. Zhang, L. Bruhwiler, and A. P. Barrett, "Amount and timing of permafrost carbon release in response to climate warming," *Tellus B, Chem. Phys. Meteorol.*, vol. 63, no. 2, pp. 168–180, Jan. 2011.

[10] E. A. Schuur and A. Abbott, "Climate change: High risk of permafrost thaw," *Nature*, vol. 480, pp. 32–33, Nov. 2011.

[11] M. R. Turetsky *et al.*, "Permafrost collapse is accelerating carbon release," *Nature*, vol. 569, pp. 32–34, May 2019.

[12] C. Wagner-Riddle *et al.*, "Globally important nitrous oxide emissions from croplands induced by freeze–thaw cycles," *Nature Geosci.*, vol. 10, pp. 279–283, 2017.

[13] Y. Sun *et al.*, "Determining in-situ soil freeze–thaw cycle dynamics using an access tube-based dielectric sensor," *Geoderma*, vol. 189, pp. 321–327, Nov. 2012.

[14] X. Chen, L. Liu, and A. Bartsch, "Detecting soil freeze/thaw onsets in Alaska using SMAP and ASCAT data," *Remote Sens. Environ.*, vol. vol. 220, pp. 59–70, Jan. 2019.

[15] D. Entekhabi *et al.*, "The soil moisture active passive (SMAP) mission," *Proc. IEEE*, vol. 5, no. 98, pp. 704–716, May 2010.

[16] J. Tao *et al.*, "Permafrost variability over the Northern Hemisphere based on the MERRA-2 reanalysis," *Cryosphere*, vol. 13, no. 8, pp. 2087–2110, Aug. 2019.

[17] R. H. Chen, A. Tabatabaeenejad, and M. Moghaddam, "Retrieval of permafrost active layer properties using time-series P-band radar observations," *IEEE Trans. Geosci. Remote Sens.*, vol. 57, no. 8, pp. 6037–6054, Aug. 2019.

[18] J. Cohen *et al.*, "A modeling-based approach for soil frost detection in the northern boreal forest region with C-Band SAR," *IEEE Trans. Geosci. Remote Sens.*, vol. 57, no. 2, pp. 1069–1083, Sep. 2018.

[19] K. Böttcher *et al.*, "Proxy indicators for mapping the end of the vegetation active period in boreal forests inferred from satellite-observed soil freeze and ERA-Interim reanalysis air temperature," *J. Photogramm. Remote Sens. Geoinf. Sci.*, vol. 86, no. 3/4, pp. 169–185, Oct. 2019.

[20] X. Wu and S. Jin, "Can we monitor the bare soil freeze-thaw process using GNSS-R?: A simulation study," *Proc. SPIE*, vol. 9264, Nov. 2014, Art. no. 92640I.

[21] S.-E. Park, A. Bartsch, D. Sabel, W. Wagner, V. Naeimi, and Y. Yamaguchi, "Monitoring freeze/thaw cycles using ENVISAT ASAR Global Mode," *Remote Sens. Environ.*, vol. 115, no. 12, pp. 3457–3467, 2011.

[22] C. Derksen, T. A. Black, E. Euskirchen, A. Langlois, M. M. Loranty, and P. Marsh, "Retrieving landscape freeze/thaw state from Soil Moisture Active Passive (SMAP) radar and radiometer measurements," *Remote Sens. Environ.*, vol. 194, pp. 48–62, Jun. 2017.

[23] V. U. Zavorotny, S. Gleason, E. Cardellach, and A. Camps, "Tutorial on remote sensing using GNSS bistatic radar of opportunity." *IEEE Geosci. Remote Sens. Mag.*, vol. 2, no. 4, pp. 8–45, Dec. 2014.

[24] M. Unwin *et al.*., "Spaceborne GNSS-reflectometry on TechDemoSat-1: Early mission operations and exploitation," *IEEE J. Sel. Topics Appl. Earth Obs. Remote Sens.*, vol. 9, no. 10, pp. 4525–4539, Sep. 2016.

[25] C. S. Ruf *et al.*, "A new paradigm in earth environmental monitoring with the CYGNSS small satellite constellation," *Sci. Rep.* vol. 8, Jun. 2018, Art. no. 8782.

[26] H. Carreno-Luengo, G. Luzi, and M. Crosetto, "Sensitivity of CyGNSS bistatic reflectivity and SMAP microwave radiometry brightness temperature to geophysical parameters over land surfaces," *IEEE J. Sel. Topics Appl. Earth Observ. Remote Sens.*, vol. 12, no. 1, pp. 107–122, Aug. 2018.

[27] S. Kraatz *et al.*, "Evaluation of SMAP freeze/thaw retrieval accuracy at core validation sites in the contiguous United States," *Remote Sens.*, vol. 10, no. 9, pp. 1483, Sep. 2018.

[28] C. Chew *et al.*, "SMAP radar receiver measures land surface freeze/thaw state through capture of forward-scattered L-band signals," *Remote Sens. Environ.*, vol. 198, pp. 333–344, 2017.

[29] M. P. Clarizia and C. S. Ruf, "On the spatial resolution of GNSS reflectometry," *IEEE Geosci. Remote Sens. Lett.*, vol. 13, no. 8, pp. 1064–1068, Jun. 2016.

[30] A. Camps, "Spatial resolution in GNSS-R under coherent scattering," *Geosci. Remote Sens. Lett.*, vol. 17, no. 1, pp. 32–36, Jan. 2020.

[31] D. Comite, F. Ticconi, L. Dente, L. Guerriero, and N. Pierdicca, "Bistatic coherent scattering from rough soils with application to GNSS reflectometry," *IEEE Trans. Geosci. Remote Sens.*, vol. 58, no. 1, pp. 612–625, Oct. 2019.

[32] C. Chew *et al.*, "Demonstrating soil moisture remote sensing with observations from the UK TechDemoSat-1 satellite mission," *Geophysical Res. Lett.*, vol. 16, no. 7, pp. 3317–3324, Apr. 2016.

[33] H. Park *et al.*, "A generic level 1 simulator for spaceborne GNSS-R Missions and application to Geros-ISS ocean reflectometry," *IEEE J. Sel. Topics Appl. Earth Observ. Remote Sens.*, vol. 10, no. 10, pp. 4645–4659, Oct. 2017.

[34] W. Li, E. Cardellach, F. Fabra, S. Ribó, and A. Rius, "Applications of spaceborne GNSS-R over inland waters and wetlands," *Proc. IEEE Int. Geosci. Remote Sens. Symp.* 2019, pp. 5255–5258.

[35] C. Gerlein-Safdi and C. S. Ruf, "A CYGNSS-based algorithm for the detection of inland waterbodies," *Geophysical Res. Lett.*, vol. 46, pp. 12065–12072, 2019.

[36] L. Dente, L. Guerriero, D. Comite, and N. Pierdicca, "Space-borne GNSS-R signal over a complex topography: Modelling and validation," *IEEE J. Sel. Topics Appl. Earth Observ. Remote Sens.*, vol. 13, pp. 1218–1233, Mar. 2020.

[37] F. Fabra, E. Cardellach, W. Li, and A. Rius, "WAVPY: A GNSS-R open source software library for data analysis and simulation," in *Proc. IEEE Int. Geosci. Remote Sens. Symp.*, 2017, pp. 4125–4128.

[38] M. Kurum *et al.*, "SCoBi-Veg: A generalized bistatic scattering model of reflectometry from vegetation for signals of opportunity applications," *IEEE Trans. Geosci. Remote Sens.*, vol. 57, no. 2, pp. 1049–1068, Feb. 2019.

[39] H. Carreno-Luengo, S. Lowe, C. Zuffada, S. Esterhuizen, and S. Oveisgharan, "Spaceborne GNSS-R from the SMAP mission: First assessment of polarimetric scatterometry over land and cryosphere," *Remote Sens.*, vol. 9, no. 4, Apr. 2017, Art. no. 362.

[40] N. Rodriguez-Alvarez, S. Misra, E. Podest, M. Morris, and X. Bosch-Lluis, "The use of SMAP-reflectometry in science applications: Calibration and capabilities," *Remote Sens.*, vol. 11, no. 20, Jan. 2019, Art. no. 2442.

[41] E. Cardellach et al.*et al.*, "GNSS transpolar Earth reflectometry exploring system (G-TERN): Mission concept," *IEEE Access*, vol. 6, pp. 13980–14018, Mar. 2018.

[42] A. Camps, H. Park, G. Portal, and L. Rossato, "Sensitivity of TDS-1 GNSS-R reflectivity to soil moisture: Global and regional differences and impact of different spatial scales," *Remote Sens*., vol. 10, no. 11, Nov. 2018, Art. no. 1856.

[43] N. Pierdicca *et al.*, "Spaceborne GNSS reflectometry data for land applications: An analysis of techdemosat data," in *Proc. IEEE Int. Geosci. Remote Sens. Symp.*, Jul. 2018, pp. 3343–3346.

[44] A. M. Balakhder, M. M. Al-Khaldi, and J. T. Johnson, "On the coherency of ocean and land surface specular scattering for GNSS-R and signals of opportunity systems," *IEEE Trans. Geosci. Remote Sens.*, vol. 57, no. 12, pp. 10426–1036, Sep. 2019.

[45] T. Wang, C. Ruf, B. Block, D. McKague, and S. Gleason, "Design and performance of a GPS constellation power monitor system for improved CYGNSS L1B calibration," *IEEE J. Sel. Topics Appl. Earth Observ. Remote Sens.*, vol. 12, no. 1, pp. 26–36, Jan. 2019.

[46] P. E. O'Neill, S. Chan, E. G. Njoku, T. Jackson, and R. Bindlish, "SMAP L3 Radiometer Global Daily 36 km EASE-Grid Soil Moisture," Version 5, NASA National Snow and Ice Data Center Distributed. Active Archive Center, Boulder, CO, USA, 2018. doi: https://doi.org/10.5067/ZX7YX2Y2LHEB. Accessed: Nov. 26, 2019.

[47] E. Tetlock, B. Toth, A. Berg, T. Rowlandson, and J. T. Ambadan, "An 11-year (2007–2017) soil moisture and precipitation dataset from the Kenaston Network in the Brightwater Creek basin, Saskatchewan, Canada," *Earth Syst. Sci. Data*, vol. 11, no. 2, pp. 787–796, 2019.

[48] J. Ikonen et al.*et al.*, "The Sodankylä in situ soil moisture observation network: An example application of ESA CCI soil moisture product evaluation," *Geosci. Instrum. Methods Data Syst.*, vol. 5, pp. 95–108, Apr. 2016.

[49] S. Channan *et al.*, "Global mosaics of the standard MODIS land cover type data," Univ. Maryland, Pacific Northwest National Laboratory, College Park, MD, USA, 2014.

[50] "Soil moisture active passive (SMAP): Algorithm theoretical basis document level 2 & 3 soil moisture (passive) data products," Revision D, Jun. 6, 2018. [Online]. Available: https://nsidc.org/data/SPL3SMP/versions/5, Accesed: Nov. 26, 2019.

[51] X. Xu et al.*et al.*, "SMAP L3 radiometer global and northern hemisphere daily 36 km EASE-grid freeze/thaw state," version 2 ed., Boulder, CO, USA, NASA National Snow and Ice Data Center. [Online]. Available: https://nsidc.org/data/SPL3FTP/versions/2, Accessed: Nov. 26, 2019.

[52] G. H. Allen and T. M. Pavelsky, "Global extent of rivers and streams," *Science*, vol. 361, no. 6402, pp. 585–588, Aug. 2018.

[53] 2020. [Online]. Available: https://proba-v-mep.esa.int/applications/time-series-viewer/app/app.html

Davide Comite (Senior Member, IEEE) received the master's degree (*cum laude*) in telecommunications engineering in 2011 and the Ph.D. degree in electromagnetics and mathematical models for engineering in 2015, both from "Sapienza" University, Rome, Italy.

He was a Visiting Ph.D. Student with the Institute of Electronics and Telecommunications of Rennes, University of Rennes 1, France, from March to June 2014. He was a Postdoctoral Researcher with the Center of Advanced Communications, Villanova University, PA, USA, from April to December 2015. He is currently a Postdoctoral Researcher with "Sapienza" University, Rome, Italy. His scientific interests include the study of the scattering from natural surfaces as well as the GNSS reflectometry over land, radar altimetry for biomass monitoring, the microwave imaging and objects detection performed through GPR, and the modeling of the radar signature in forward scatter radar systems. He is also interested in the study and design of microwaves and millimetre-waves antennas and leaky-wave antennas, and in the generation of nondiffracting waves and pulses.

Dr. Comite has been a recipient of a number of awards at national and international conferences. Most recently, he has received a Young Scientist Award for the URSI GASS 2020. He received the *Publons Top Peer Reviewers Award* for both *Geoscience and Engineering* in September 2018, and for Cross-fields in 2019. In 2019, the IEEE Antennas and Propagation Society recognized him as an Outstanding Reviewer for the IEEE TRANSACTION ON ANTENNAS AND PROPAGATION. In 2020, he was awarded as the Best Reviewer for the IEEE JOURNAL OF SELECTED TOPICS IN APPLIED EARTH OBSERVATION AND REMOTE SENSING. He currently serves as a Reviewer for several international journals. He is an Associate Editor of the IET Journal of Engineering, the IET Microwaves, Antennas and Propagation by the Institution of Engineering and Technology, and IEEE ACCESS. He is an URSI Senior Member.

Luca Cenci was born in Rome (Italy), in 1986. He received the B.S. degree (*cum laude*) in "Coordination of Civil Protection Activities" from the University of Perugia, Perugia, Italy, in 2010; the M.S. degree (*cum laude*) in "Geosciences and Geotechnologies" from the University of Siena, Siena, Italy, in 2013; the Ph.D. degree (grade: Excellent) in "Understanding and Managing Extremes" ("Weather-Related Risk" University School for Advanced Studies IUSS Pavia, Pavia, Italy, in 2016.

He was a Visiting Student with the University of Malta and a Trainee in the Malta Civil Protection Department, in Malta, in 2009. He was a Visiting Student with the Department of Environment and Planning, University of Aveiro, Portugal, in 2012. He was a Trainee with the Geomatics Laboratory of the Centre for GeoTechnologies (CGT) - University of Siena, San Giovanni Valdarno (AR), Italy, in 2013. He was a Visiting Researcher with the Luxembourg Institute of Science and Technology (LIST), Luxembourg, in 2016. From 2014 to 2019, he was a Researcher with CIMA Research Foundation, Savona, Italy. From 2017 to 2019, he was a Postdoctoral Researcher with the Department of Information Engineering, Electronics and Telecommunications, Sapienza University of Rome, Rome, Serco Italia SpA, Frascati, Italy a Science Support Specialist and Earth Observation (EO) Products Analysis Expert for the Copernicus Coordinated Data Quality Control (CQC) service. His main research interests include Optical & SAR remote sensing data processing and quality assessment; EO & GIS applications for environmental analyses, with a particular emphasis on: geosciences (mainly, hydrology and geology), natural hazards and disaster risk management.

Mr. Cenci received the "Premio Nazionale di Laurea Eugenio Zilioli" for the best Italian Master's Thesis on remote sensing by the National Research Council (CNR) of Italy Institute for Electromagnetic Sensing of the Environment (IREA) and the Federation of Scientific Associations for Territorial and Environmental Information (ASITA) in 2013.

Andreas Colliander (Senior Member, IEEE) received the M.Sc. (Tech.), Lic.Sc. (Tech.), and D.Sc. (Tech.) degrees from Aalto University, Espoo, Finland, in 2002, 2005, and 2007, respectively.

He is currently a Research Scientist with NASA Jet Propulsion Laboratory, California Institute of Technology, Pasadena, CA, USA.

Dr. Colliander is a member of the Science Algorithm Development Team for the Soil Moisture Active Passive Mission, focusing on the calibration and validation of the geophysical products.

Nazzareno Pierdicca (Senior Member, IEEE) received the Laurea (Doctor's) (*cum laude*) degree in electronic engineering from the University "La Sapienza" of Rome, Rome, Italy, in 1981.

From 1978 to 1982, he was with the Italian Agency for Alternative Energy. From 1982 to 1990, he was with Telespazio, Rome, Italy, in the Remote Sensing Division. In November 1990, he joined the Department of Information Engineering, Electronics and Telecommunications, Sapienza University of Rome. He is currently a Full Professor and teaches remote sensing with the Faculty of Engineering, Sapienza University of Rome, Rome, Italy. His research interests include electromagnetic scattering and emission models for sea and bare soil surfaces and their inversion, microwave radiometry of the atmosphere, and radar land applications.

Prof. Pierdicca is the past Chairman of the GRSS Central Italy Chapter.